Journal of Manufacturing Processes 67 (2021) 438–446

Contents lists available at ScienceDirect

Journal of Manufacturing Processes

journal homepage: www.elsevier.com/locate/manpro

Feasibility study of producing multi-metal parts by Fused Filament Fabrication (FFF) technique

Mehrdad Mousapour [a,*], Mika Salmi [a], Lassi Klemettinen [b], Jouni Partanen [a]

[a] Department of Mechanical Engineering, Aalto University, Otakaari 4, 02150, Espoo, Finland
[b] Department of Chemical and Metallurgical Engineering, Aalto University, Kemistintie 1, 02150, Espoo, Finland

ARTICLE INFO

Keywords:
3D printing
Fused filament fabrication (FFF)
Material extrusion (MEX)
Multi-metal additive manufacturing
Fused deposition modeling (FDM)

ABSTRACT

Additive manufacturing, or more commonly 3D printing, has been recently established as one of the most advanced technologies for fabricating multi-material parts. In this work, the possibility of manufacturing multi-metal parts by material extrusion process was studied for the first time. Three types of samples, named mixed, coupled and graded, resulting from deposition of two ferrous alloys: high carbon iron and stainless steel 316 L filaments, were successfully printed. After de-binding with different heating rates, they were isothermally sintered in the range of 1310−1400 °C for various holding times in argon atmosphere. Finally, some properties of the final parts, such as relative density, shrinkage, microstructural evolution, and hardness were analyzed. In conclusion, the relative density was measured up to 92 %, and the shrinkage recorded for the samples ranged between 10 % and 40 %. Based on the performed analyses, a relatively homogeneous microstructure was observed in the mixed sample, which indicates that the affordable metal extrusion technique could replace the conventional methods for metallic alloying.

1. Introduction

Additive manufacturing (AM) technologies, in the recent decades, have considerably expanded their applications in various fields due to their unique benefits such as producing parts with complex geometries [1,2] and reducing production time and costs [3–5]. One of the methods in AM is Material extrusion, which was first commercialized as fused deposition modeling (FDM) by the company Stratasys in the 1990's, and then also known as Fused filament fabrication (FFF). This technique is about the deposition of melted filaments through a nozzle to produce a 3D part layer by layer [6,7]. The most benefit of using FFF is affordability and availability of this technology. In fact, FFF is a useful method for producing complex shape parts using simple home printers with very low production costs [8,9]. Also, it has been claimed that manufacturing presentation models and rapid prototype parts can be considered as the largest applications of FFF [10]. As well as this, other applications have been recently growing in AM markets such as spare parts [11,12] and medical parts [13–16].

Although FFF is mostly considered as a method for production of plastic parts, a few attempts have been conducted to fabricate the other types of materials including ceramics and metals using this technique [17–24]. In this method, a mixture of various metallic/ceramic powders and a polymeric binder can be used in the form of feedstock filament materials. However, there are still some limitations, especially regarding the range of nozzle diameter. Giberti et al. [17] stated that powder volume fraction is a critical factor, which has an effective role in successful production of ceramic/metal parts. Recently, Thompson et al. [18] studied 316 L stainless steel parts produced by FFF using a filament with 55 vol.% steel powder. They successfully reported the optimized production (e.g. printing, debinding and sintering) parameters based on mechanical properties and densities of the final parts. In another work, Ait-Mansour et al. [19] studied the effect of design parameters including infill levels and build orientation on shrinkage and mechanical properties of final BASF Ultrafuse 316 LX. Furthermore, some research has been carried out on other metals such as stainless steel (AISI 630) [17], titanium alloys (Ti6Al4V) [20], tungsten carbide cobalt [21,22], carbonyl iron [23], and rare earth magnets [24], where these metallic parts were successfully fabricated by FFF technology.

Although a large share of studies has focused on using a single material in AM technologies, a few studies have been conducted on multi material additive manufacturing (MMAM) in order to develop the functionality of AM parts. As Vaezi et al. [25] stated, MMAM is an

* Corresponding author.
E-mail address: mehrdad.mousapour@aalto.fi (M. Mousapour).

https://doi.org/10.1016/j.jmapro.2021.05.021
Received 11 March 2021; Received in revised form 27 April 2021; Accepted 6 May 2021
Available online 17 May 2021

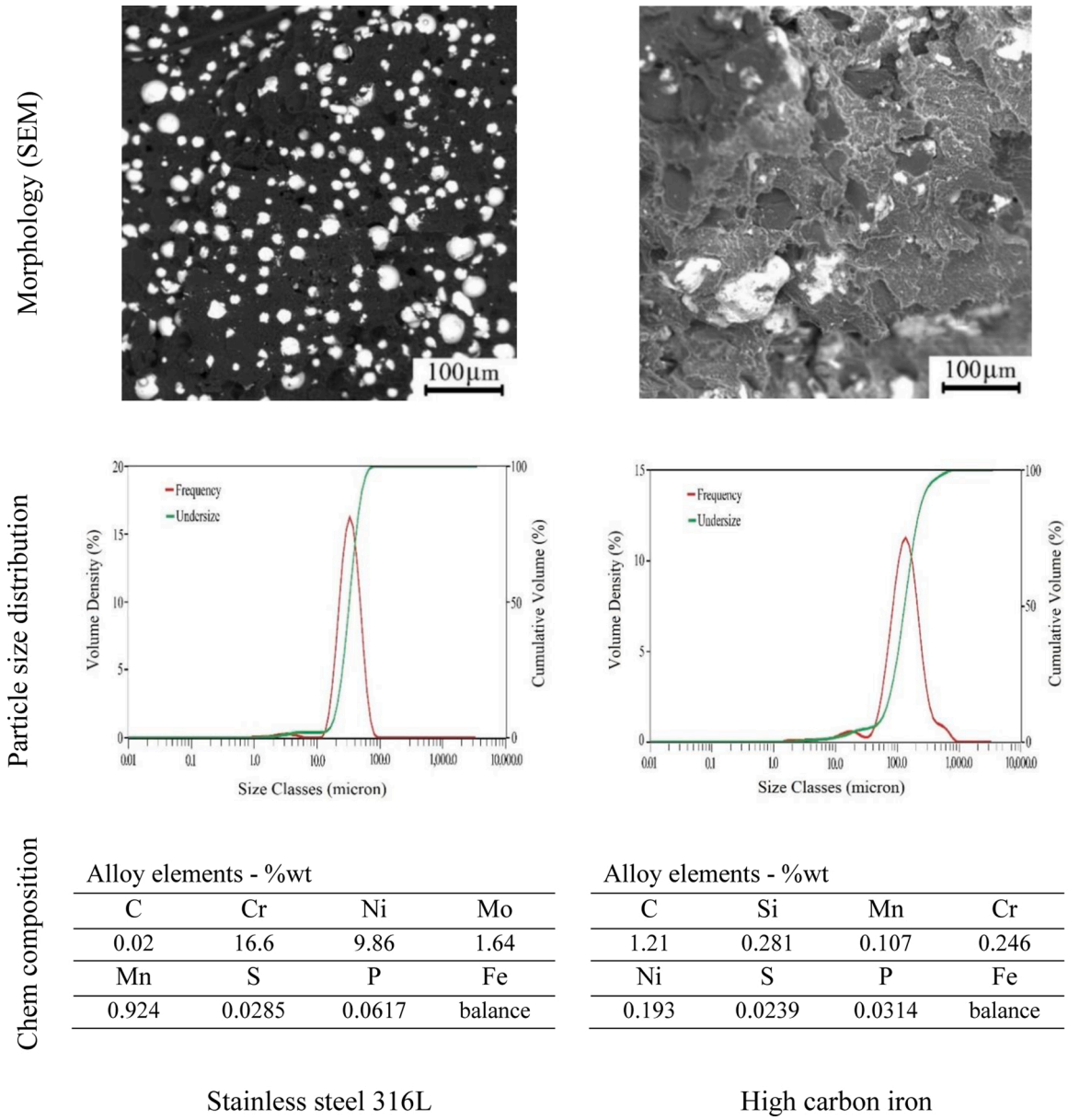

Fig. 1. Characteristics of metal particles of raw materials.

affordable package to produce valuable parts with high performance properties, due to the possibility of utilizing different materials in each layer of printed parts. In another publication, Bandyopadhyay and Heer [26] suggested that joining different metal parts by traditional multi-step welding process could be replaced by functionally graded materials (FGM) in which several metals can be deposited in a single layer. A few attempts have been made to fabricate multi-metal parts such as In718-Ti6Al4V, In718-Cu, SS316-SS430, SS316-Ti6Al4V-NiCr, Ti6Al4V-CoCrMo [27–29] and Ti6Al4V-Ti-Al, Ti6Al4V-Nb [30–33] alloys by directed energy deposition (DED, laser engineering net shaping LENS). Some other suitable techniques for fabrication of multi-metal parts include powder bed fusion methods, such as direct metal laser melting (DMLM) and electron beam melting (EBM). There are, however, some challenges in the fabrication of multi-metal parts, such as unpredictable properties due to non-isotropic nature of the components, manufacturing of larger-scale parts, material selection, and possibly high production costs, which limit the use of some AM technologies [26, 34]. The aim of this study was producing different types of multi-metal parts by FFF technology. In order to simplify the analysis of the produced parts, only two metallic filaments were used in this study. Since FFF is an affordable technique, analyzing physical and mechanical properties of the final parts manufactured by cheap home-printers would be interesting. This paper evaluates the possibility of using this process as a novel approach for manufacturing a metallic alloy.

2. Material and methods

2.1. Raw materials

Two metallic filaments used in this study were stainless steel 316 L and high carbon iron, which were manufactured by The Virtual Foundry company. These types of filaments, which are commercially called Filamet™, contained PLA as the binder and an extremely high metal powder content. The stainless steel 316 L filament had a density of 3.5 g/cm^3 and metal content of 83.5 wt-%, while these values for high carbon iron filament were 2.75 g/cm^3 and 80 wt-%, respectively. In order to characterize the raw materials, the morphology, particle size distribution, and chemical composition of both filaments used (metal

Table 1
Print settings used for multi-metal samples.

Nozzle temperature	210 °C	Bed temperature	60 °C
Infill density	100 %	Printing speed	15 mm/s
Diameter of deposited material	0.8 mm	Line width	0.7 mm
Layer thickness	0.2 mm	First layer thickness	0.53 mm

particles) were analyzed. Fig. 1 indicates the characteristics of both materials.

According to the results of particle size distribution, stainless steel 316 L powder had the range of 0.872−76 μm and the median (d_{50}) of 32.7 μm, while this range for high carbon iron was measured to be 1.45−756 μm, where d_{50} was 129 μm. Based on the measurements, it was obvious that stainless steel 316 L particles were smaller than that of high carbon iron (it is also visible in Fig. 1: morphology). The essential steps in the manufacturing chain of a multi-metal part by FFF are expressed in the following sub-chapters.

2.2. Printing

The Crane Quad 3D machine (M3D, MD, USA) was used to print the samples. Although the printer was able to take in four filaments, the number of extruders used in this study was two. In this printer, the filaments were mixed in the nozzle chamber and the combined material extruded on the bed. Three types of samples including: a) mixed sample (50−50), b) coupled sample, and c) functionally graded sample, with dimensions of 10 × 10 × 10 mm were designed by Cura 4.4.1. The models were printed based on the parameters given in Table 1, where the size of prints were 10.56 × 10.52 × 9.82 ± 0.05 mm. Fig. 2 shows a schematic representation of each sample type.

2.3. Debinding

Based on the type of Filamet™ [35], the binder was completely removed by heat treating at a specific temperature and time. In order to determine the appropriate conditions for de-binding, the mass loss of samples was recorded by using thermogravimetric analysis (TGA) technique. The sample was suspended in a furnace (Heraeus) by a platinum wire attached to a digital balance (Mettler Toledo: AB104-S/0.1 mg accuracy) in Ar atmosphere. The TGA results were used to set the de-binding temperature and holding time for the main tests.

2.4. Sintering

The sintering process was carried out directly after de-binding in the same vertical 16/450 laboratory furnace (Lenton, Parsons Lane, Hope, UK) with no change in the position of the sample nor the gas atmosphere. The temperature was recorded with a calibrated S-type Pt/Pt10Rh thermocouple (Johnson Matthey, London, UK) connected to multimeters (models 2000 and 2010, Keithley, Solon, OH, USA). The sample was located in the middle of a cylindrical-shaped magnesia crucible, and this setup inserted into the furnace using a molybdenum crucible holder supported by an alumina rod. A schematic figure of the furnace set-up has been presented previously in another publication [36]. In this study, the whole thermal process was conducted in argon atmosphere (AgA-Linde, Finland; purity 99.997 %) with a flow rate of 0.28 L/min (controlled by a mass flow controller, Aalborg, NY, USA). The sample, located inside the magnesia crucible, was completely covered (buried) in refractory ballast powder (including Al_2O_3, CaO, and SiO_2) for more protection from oxidation. After de-binding, the samples were heated with the rate of 5 °C/min up to the target sintering temperatures between 1310 and 1400 °C, and sintered for 1 h, 6 h and 12 h. After the desired holding time, the sample – crucible assembly was carefully lowered from the hot-zone of the furnace in five steps to obtain as high cooling rate as possible while simultaneously minimizing the thermal shock to the furnace work tube. The inert argon atmosphere was maintained during the cooling process. The time for cooling from ~1360 °C to room temperature was approximately 45 min, corresponding to a cooling rate of 30 °C/min. The sintered samples were analyzed to monitor the properties and characteristics of the final fabricated multi-metal parts. Accordingly, the sintered density was measured by Archimedes method (DIN ISO 3369) for each sample to express the degree of densification. This parameter was reported as "relative sintering", which defined as the ratio of sintered to theoretical density, where theoretical density is expressed as:

$$\frac{1}{\rho_{th}} = \sum_{i}^{N} \frac{w_i}{\rho_i} \tag{1}$$

where, w_i is the mass fraction of each element, ρ_i the theoretical density of i_{th} element and N is the number of elements in the alloy. The shrinkage amount of samples during the process was investigated by analyzing the samples' dimensions before and after sintering. Therefore, the dimensional change profiles were plotted by measurement of sample dimensions using Screen Ruler 2D software. In this method, the measurement was done by a ruler from the taken images from both sintered and green samples. In order to monitor the porosity and elemental distribution in microstructure, elemental mapping and point/area analyses were performed using a scanning electron microscope (SEM; Mira3, Tescan, Czech Republic) equipped with an energy dispersive spectrometer (EDS; Thermo Fisher Scientific, USA). An optical microscope (Olympus BH-2, Tokyo, Japan) was also used for imaging the samples. Furthermore, X-ray diffraction (XRD; Malvern Panalytical X'Pert Pro MPD Powder, UK) analysis was used to characterize the types of phases and compounds that might be formed during sintering. The particle size distribution of the raw materials was studied (by Malvern Mastersizer 3000, UK) based on ISO 31320. In order to analyze mechanical properties of the sintered samples, Vickers micro hardness analysis was carried out on the cross section of each sample by a tester (Innovatest Nexus 4303, Netherlands) with a load of 196.1 mN and 10 s dwell time.

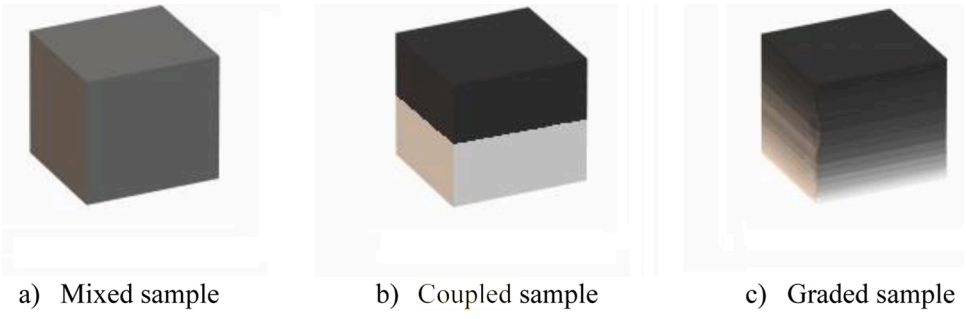

Fig. 2. Schematic representations of three types of multi-metal parts: a) mixed sample (50-50), b) coupled sample (100-100), c) functionally graded sample (0-100).

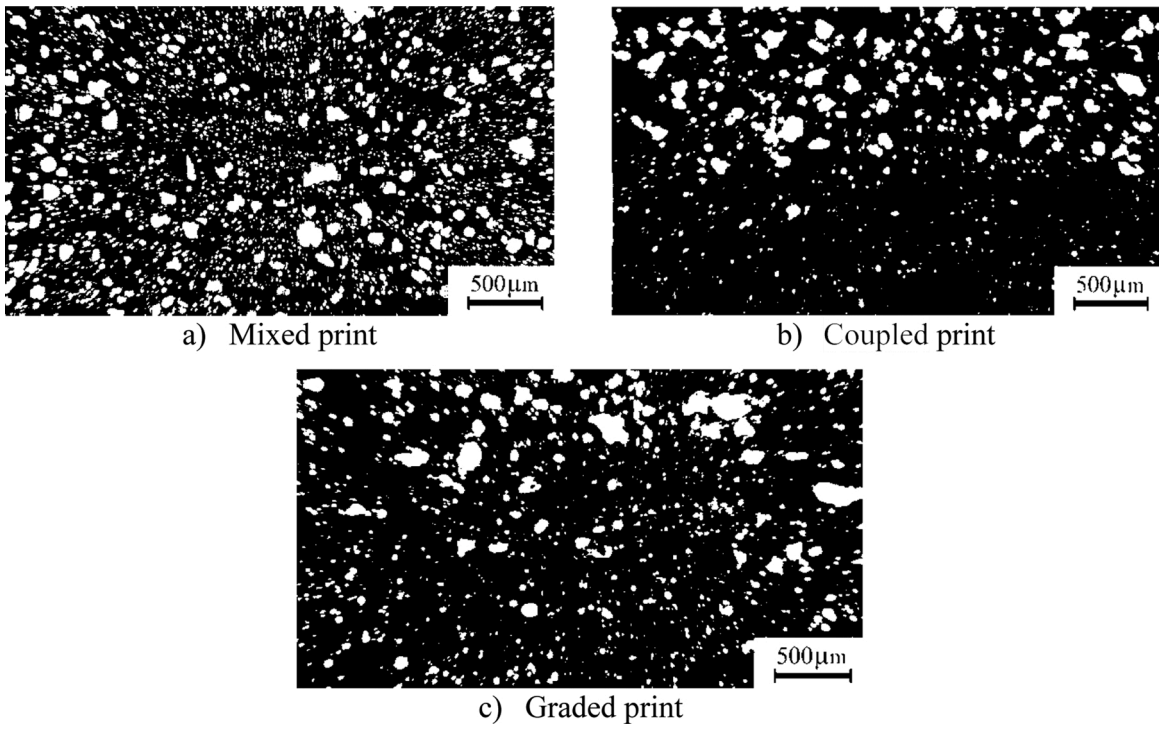

Fig. 3. Optical microscope images taken from the cross sections of the three different types of prints.

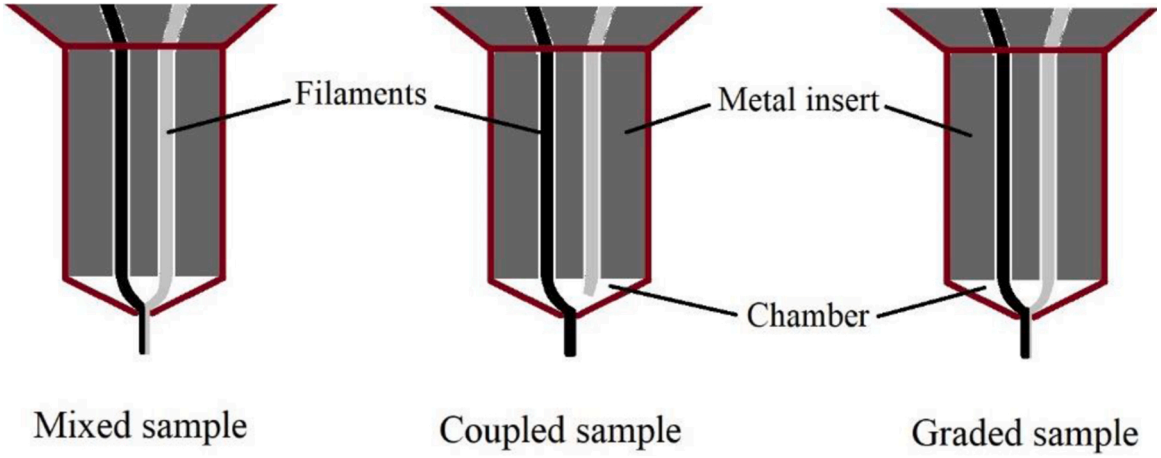

Fig. 4. A schematic of nozzle and mixing process of extruded filaments in the chamber.

3. Results and discussion

In order to investigate the microstructures of the three types of prints in larger scale, optical microscope images from cross-sections of each print were taken and are presented in Fig. 3 a–c. As seen in Fig. 3a, the structure of the mixed print is generally homogenous, i.e. the 316 L and high carbon iron particles are evenly distributed throughout the sample. In the coupled print (Fig. 3 b), the difference in particle types of stainless steel 316 L and high carbon iron is recognizable. Fig. 3 c shows the two materials graded from bottom to top, however in reality it is not feasible to achieve 0–100 % grading. In fact, since the mixing process of filaments occurs in the chamber, a part of filament A is deposited alongside filament B. Due to this, the share of high carbon iron particles (filament B) at the topmost layer of the print would be around 90 % instead of 100 %. Fig. 4 shows a schematic of the nozzle in which two filaments are mixed in and extruded from the chamber. In fact, the extruded material from the nozzle contains two different components side by side with a distinct interface.

To measure the mass change of the printed samples, a Thermogravimetric Analysis (TGA) test was conducted in order to determine the decomposition behavior of the PLA. The prints were heated from ambient temperature to 250 °C with 5 °C/min, and then up to 400 °C with 1 °C/min. The temperature remained constant at 400 °C, until no further mass changes were observed. Fig. 5 shows the mass loss of the print as a function of de-binding process time, measured by the TGA test. This graph shows that the majority of the polymer decomposition occurs between 250 °C and 400 °C. According to the TGA result, heating up to 400 °C and holding for maximum one hour would be sufficient to eliminate all the PLA (~20 wt.%) from the prints. Therefore, this heating program was used for all three types of prints in the de-binding stage.

After de-binding, the prints were isothermally sintered at various sintering temperatures and times. First, the sintered density was measured with the Archimedes method to determine the most desirable sintering conditions for the mixed sample. Then, the optimum

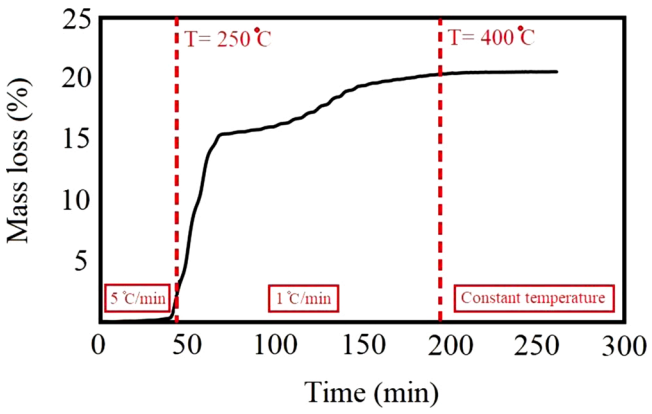

Fig. 5. The mass change of the print as a function of time during de-binding process.

parameters were applied for the other two types of samples. The relative density evolution of the mixed samples at different sintering conditions is shown in Fig. 6. The density increases as a function of increasing temperature up to 1360 °C, after which it begins to decrease. The reason of density reduction was formation of huge pores in the microstructure during sintering at temperatures higher than 1360 °C. Therefore, according to the measured data in Fig. 6 a, the highest density value was obtained at 1360 °C. To investigate the effect of time on the relative density, sintering experiments were also carried out with longer holding times at 1360 °C (optimum temperature). As the holding time was prolonged from 1 to 12 h, the relative density value increased from 87 % to 90 % (black dots and line in Fig. 6 b). According to Thompson et al. [18], the heating rate of de-binding process can directly affect the measured density of sintered parts. Therefore, three different heating rates (0.2, 0.7 and 1 °C/min) were tested at the temperature range previously established (250–400 °C). Fig. 6 b shows the relative density values obtained for these three heating rates for the mixed sample sintered at 1360 °C for 6 h. Based on the results, the optimum properties were observed at 0.2 °C/min de-binding rate, where approximately 92 % of the theoretical density was achieved. It should be noted that at such low heating rates, the temperature in the furnace did not increase linearly but rather in small steps. Fig. 7 shows optical microscope images of the mixed sample debound with different heating rates; the decrease in porosity is clearly visible. The coupled and graded samples were also sintered in the same sintering conditions (1360 °C – 6 h – 0.2 °C/min), and the relative densities were measured at 91 % and 92 %, respectively.

In order to study the apparent shape evolution and shrinkage level, the dimensions of the samples were measured and plotted after sintering in optimum conditions. Fig. 8 shows the dimensional profiles of three samples in which the dotted line introduces the dimensions of the print (green sample), while the solid line belongs to the sintered sample. In the case of the mixed sample (Fig. 8 a), the dimensional change at the center of the sample is more than that at the top and bottom edges due to some geometric reasons. This mode, which is well known as “X-shaped” distortion, has also been observed for other materials (e.g. Cu-base alloys) [37,38].

Based on the measured dimensional changes, the amount of shrinkage in the mixed sample was measured at approximately 10 %. Unlike in the mixed sample, the dimensional change behavior is not similar at the upper and bottom zones in the coupled sample (Fig. 8 b). This difference is induced by the type of materials in each zone, as the High Carbon Iron (HCI) particles are located in the upper section and Stainless Steel (SS) 316 L at the bottom. The higher shrinkage in the upper half can be explained by the fact that HCI has a higher densification parameter than SS 316 L in the same sintering conditions. Furthermore, the particle size distribution analysis shows that HCI particles (d_{50} = 129 μm) are larger than SS 316 L particles (d_{50} = 32.7 μm). In fact, as has been described by Mousapour et al. [37], huge spaces formed between the large particles can lead to more shrinkage at HCI zone by fragmentation-rearrangement mechanism

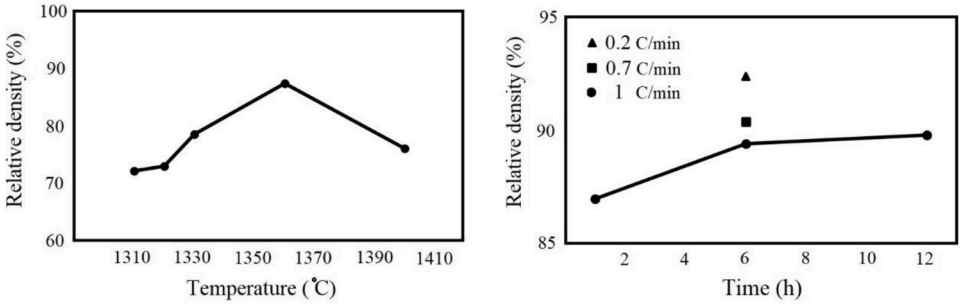

Fig. 6. The influence of target temperature, time and de-binding rate on the relative density of the mixed sample. (Theoretical density: 7.695 g/cm^3).

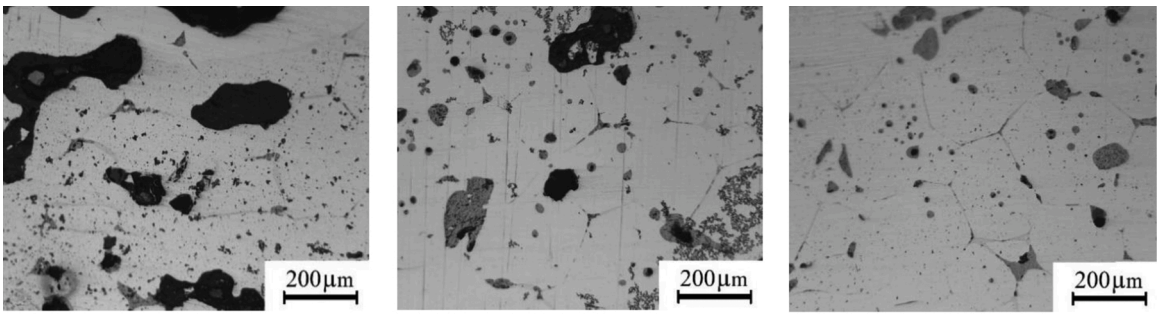

Fig. 7. OM-images of the mixed samples sintered at 1360 °C - 6 h with various de-binding rates.

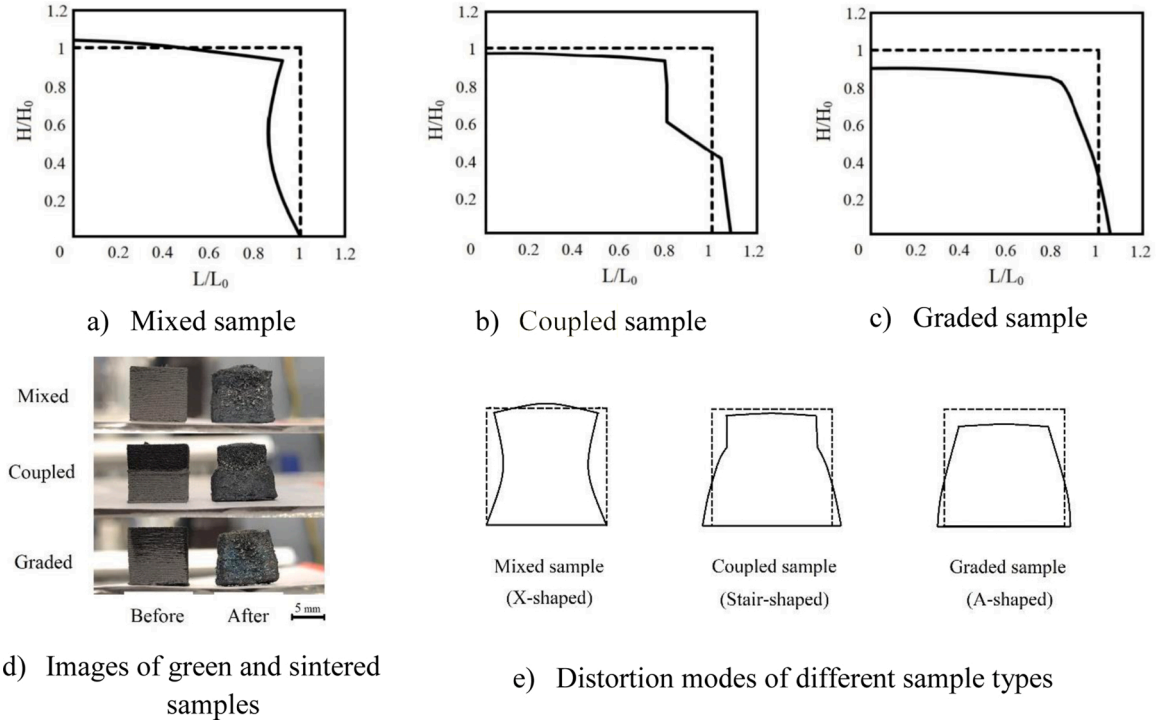

Fig. 8. The dimensional profiles of mixed (a), coupled (b), and graded (c) samples sintered at 1360 °C – 6 h - 0.2 °C/min. L/L_0 and H/H_0 are the sintered/green ratios (H_0 = 9.82 mm and L_0 = 5.28 mm). (d) the images and (e) the schematics of distortion modes before and after sintering.

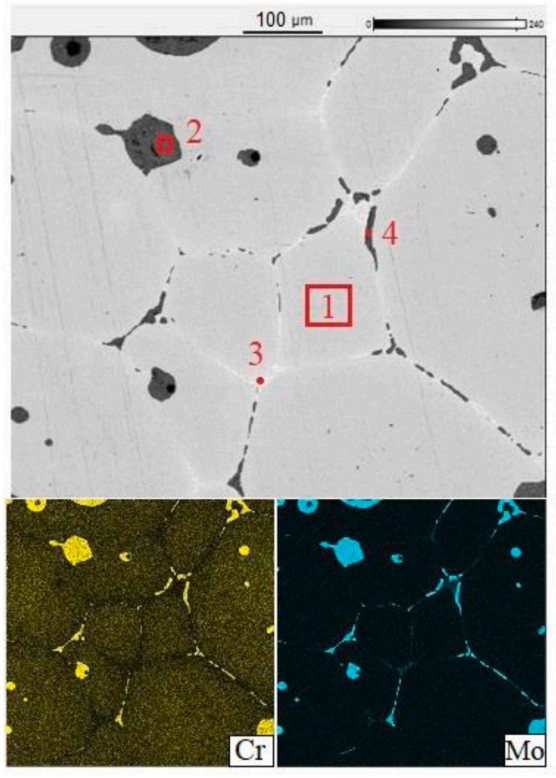

wt-%	1	2	3	4
C	2.09	1.04	2.01	1.83
Fe	78.76	17.31	67.33	4.93
Cr	6.49	27.35	0.9	35.29
Ni	10.92	0.99	12.95	0.04
Mo	1.75	52.67	16.77	57.37
Mn	-	0.65	0.03	0.53

atm-%	C	Fe	Cr	Ni	Mo	Mn
Point 4	9.99	5.77	44.42	0.05	39.14	0.63

b) EDS analysis (numbers from Fig. 9 a)

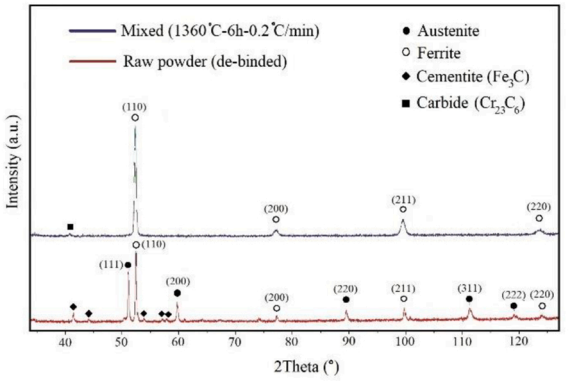

Fig. 9. The elemental distribution: (a) segregation of Cr and Mo into the grain boundaries, and (b) EDS point/area analysis in the mixed sample sintered at 1360 °C – 6 h - 0.2 °C/min, (c) XRD patterns of the mixed sample before and after sintering.

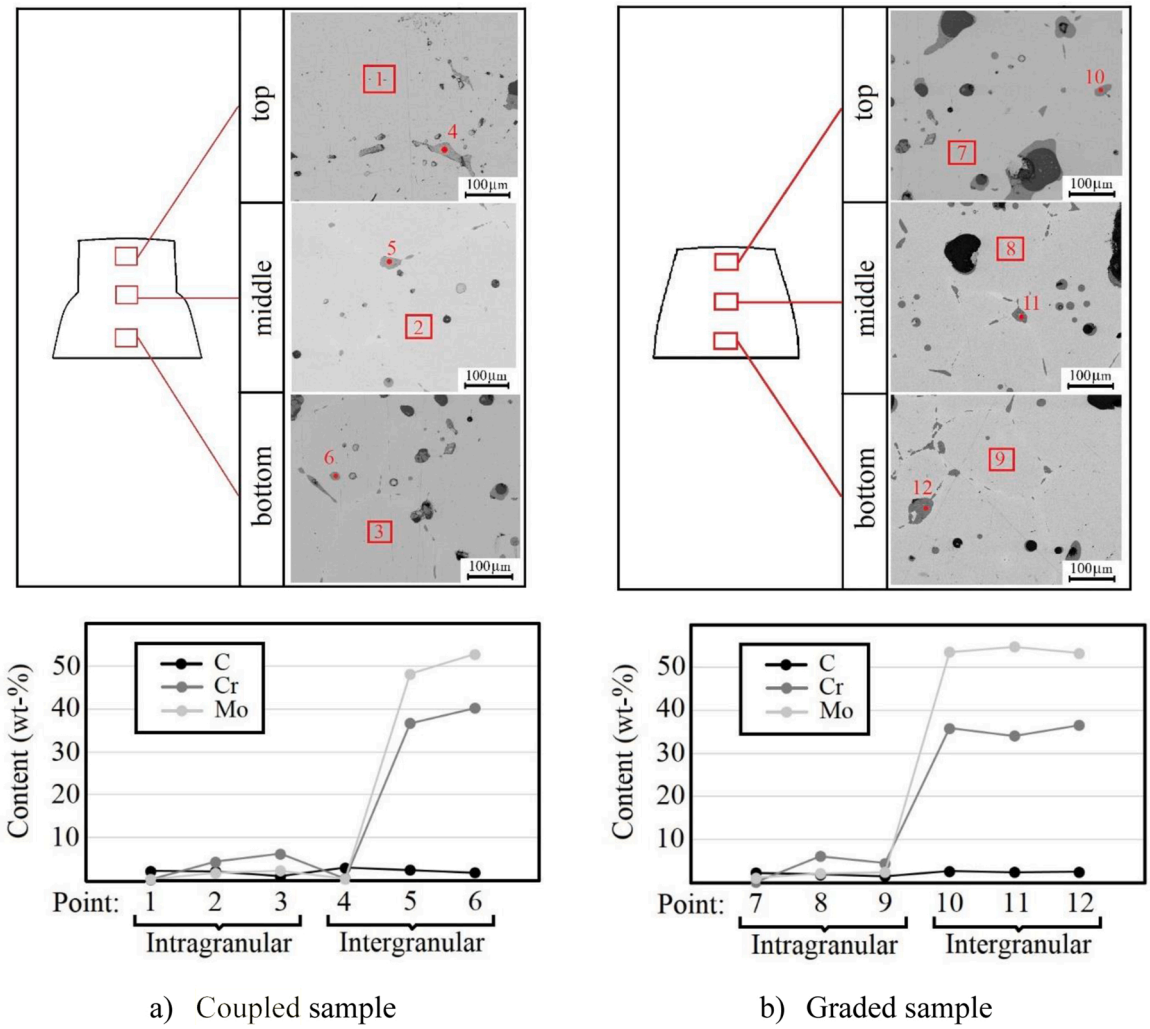

Fig. 10. EDS point/area analysis of different zones in the (a) coupled sample and (b) graded sample sintered at 1360 °C – 6 h - 0.2 °C/min. (Bottom, middle and top of cross-sections at a distance of 0.2H, 0.5H and 0.8H, respectively, where H is the height of sintered samples.).

during sintering. According to obtained data from the coupled sample, the amount of shrinkage at the upper zone was approximately 40 %, while the bottom expanded around 3 %. Due to this difference in shrinkage at the two zones, "stair-shaped" distortion was observed for this type of sample. A similar phenomenon was recorded in the graded sample, with the difference that the shrinkage level decreases gradually but uniformly from top to bottom (Fig. 8 c). This uniform change results in "A-shaped" distortion in the graded sample with a total shrinkage of 23 %. Fig. 8 d and e show images of the samples and the distortion modes before and after sintering. Since the surface quality of all three samples was not favorable enough to be directly used as the final part (due to sticking refractory powder on samples' surfaces),

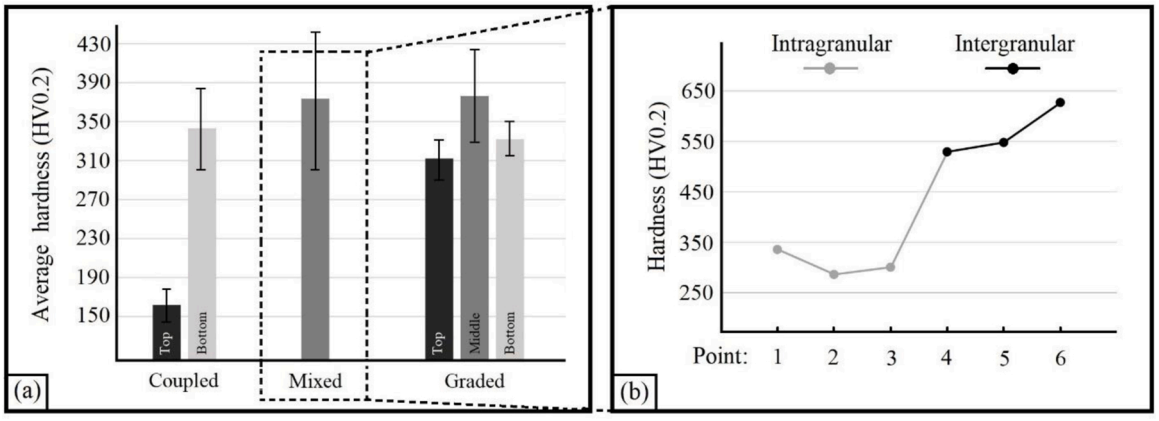

Fig. 11. (a) The average micro hardness in different zones of three samples sintered at 1360 °C – 6 h - 0.2 °C/min, and (b) micro hardness of the mixed sample measured at intragranular and intergranular points.

"post-processing" or some extra treatments, such as machining, sanding, and filing are required to prepare a final part with as high surface quality as possible. To evaluate the homogenization degree during sintering, the elemental distribution in the mixed sample was studied and results are shown in Fig. 9. EDS maps for chromium and molybdenum (both originating from SS 316 L) are shown in Fig. 9 a. According to mapping and point analyses (Fig. 9 a and b), chromium and molybdenum are segregated in various areas at the grain boundaries (Cr is precipitated in the form of $Cr_{23}C_6$). On the other side, XRD patterns of raw material powder (including both HCI and SS 316 L) and the mixed sample show a phase transformation and formation of carbide after sintering (Fig. 9 c). In the raw material powder, which was obtained from a debound print, some cementite (Fe_3C) was identified in addition to austenite and ferrite phases. The austenite and cementite peaks disappeared after sintering, and the ferrite peaks became dominant, representing a sample with full ferrite structure. It is clear that sintering at high temperatures and with long holding times is helpful in obtaining a homogeneous part, which makes FFF a possible technique for metallic alloying.

Moreover, the elemental distribution in different zones of the coupled and graded samples is shown in Fig. 10. The EDS analysis on the different zones of the coupled sample (Fig. 10 a) shows the content of C, Cr and Mo inside the grains (intragranular) and at the grain boundaries (intergranular). As it expected, C content slightly decreases from top to bottom, where there is no dramatic difference between the measured intragranular and intergranular values. Whereas, Cr and Mo contents are extremely higher at grain boundaries as a result of segregation, however, it is not observed at the top, where HCI contains low level of Chromium and Molybdenum (chemical composition in Fig. 1). Similarly, in the graded sample, precipitation of Cr and Mo at grain boundaries is evident with the difference that this also occurs at the top section due to a small amount of SS 316 L, which is mixed at this area (Fig. 10 b).

Since the coupled sample contains fully HCI at the top and SS 316 L at the bottom, comparison of each section (top and bottom) as one of the used raw materials, with the mixed sample can show the properties evolution in multi metal part after sintering. Therefore, micro hardness (HV0.2) in different zones of each sample was measured and studied in order to evaluate micro mechanical properties of all three samples (Fig. 11 a). In the case of the coupled and graded samples, the hardness measurement was conducted at 6 points in each zone so that top and bottom zones in the coupled sample (in total 12 points); and top, middle and bottom zones in the graded sample (18 points) were measured. Since the mixed sample has a uniform structure from top to bottom, only 6 points were studied, which distributed in all areas of the cross section.

In the coupled sample, which top and bottom zone represent fully HCI and SS 316 L, the average hardness is 161.3 HV0.2 and 343.21 HV0.2, respectively. This value considerably increased at the top of the graded sample to 312.35 HV0.2, where adding a small amount of SS 316 L particles resulted in a huge increment in the average hardness. On the other side, the mixed sample in which there is the same amount of both materials (also in the middle zone of the graded sample), an improvement in hardness is visible, where the highest values were recorded (373.39 ± 2.69 HV0.2). These measurements clearly evidence an enhancement of mechanical properties by alloying HCI and SS 316 L.

In order to more accurate estimation of hardness in the samples, the measurement was carried out at 3 points in each intragranular and intergranular positions. Fig. 11 b shows the micro hardness of all 6 points measured in the mixed sample. According to the results, the measured hardness at grain boundaries shows higher values than that inside the grains due to precipitation of carbides at these areas. It is in a good agreement with the EDS results shown in Fig. 9, where the hardness was measured up to 626.68 HV0.2

4. Conclusions

In this work, a feasibility study on fabrication of multi-metal parts by material extrusion technique was conducted, focusing on investigation of sintered density, apparent shape changes, and microstructural evolution. Three types of multi-metal samples, including the mixed, coupled and graded samples, were successfully printed from high carbon iron and stainless steel 316 L filaments, and after de-binding, sintered in different conditions. The results after sintering in optimal conditions (target temperature – holding time – heating rate) showed relative densities of 92 %, 91 % and 92 % for the mixed, coupled and graded samples, respectively. The investigation of apparent shape evolution of each sample during sintering shows a different shrinkage behavior, where "X-shaped", "stair-shaped" and "A-shaped" distortions were observed in the mixed, coupled and graded samples, respectively. For obtaining final multi-metal parts with high surface quality, post-processing (e.g. filing, sanding, machining, etc.) is required. According to EDS micro-analysis and XRD results, a relatively homogeneous structure was obtained in the mixed sample, which proves that alloying of high carbon iron and stainless steel 316 L with acceptable mechanical properties was successful. Consequently, the affordable FFF technology may be used as an alternative for conventional methods (e.g. powder metallurgy, mechanical alloying, etc.) to produce metal alloys with more complex geometries and lower production costs for small batches.

Declaration of Competing Interest

The authors declare that they have no known competing financial interests or personal relationships that could have appeared to influence the work reported in this paper.

Acknowledgments

This study was partly funded by Business Finland (Grant 632/31/2018), and also utilized the RawMatTERS Finland infrastructure (RAMI, Academy of Finland) based jointly at Aalto University, GTK, and VTT, Espoo.

References

[1] Jalava K, Salmi M, Kukko K, Orkas J. Multi-scale topologically optimized components made by casting and additive manufacturing. Foundry Trade J Int 2019;193:24–5.
[2] Akmal JS, Salmi M, Hemming B, Teir L, Suomalainen A, Kortesniemi M, et al. Cumulative inaccuracies in implementation of additive manufacturing through medical imaging, 3D thresholding, and 3D modeling: a case study for an end-use implant. Appl Sci 2020;10(8):2968.
[3] Gibson I, Rosen DW, Stucker B. Additive manufacturing technologies: 3d printing, rapid prototyping, and direct digital manufacturing. New York: Springer; 2014.
[4] Chekurov S, Salmi M. Additive manufacturing in offsite repair of consumer electronics. Phys Procedia 2017;89:23–30.
[5] Salmi M, Akmal JS, Pei E, Wolff J, Jaribion A, Khajavi SH. 3D printing in COVID-19: productivity estimation of the most promising open source solutions in emergency situations. Appl Sci 2020;10(11):4004.
[6] Gonzalez-Gutierrez J, Cano S, Schuschnigg S, Kukla C, Sapkota J, Holzer C. Additive manufacturing of metallic and ceramic components by the material extrusion of highly-filled polymers: a review and future perspectives. Mater 2018;11(5):840.
[7] Cuan-Urquizo E, Barocio E, Tejada-Ortigoza V, Pipes RB, Rodriguez CA, et al. Characterization of the mechanical properties of FFF structures and materials: a review on the experimental, computational and theoretical approaches. Mater 2019;12(6):895.
[8] Yang L, Hsu K, Baughman B, Godfrey D, Medina F, Menon M, et al. Additive manufacturing of metals: the technology, materials, design and production. New York: Springer; 2017.
[9] Salmi M, Ituarte IF, Chekurov S, Huotilainen E. Effect of build orientation in 3D printing production for material extrusion, material jetting, binder jetting, sheet object lamination, vat photopolymerisation, and powder bed fusion. I J C Ent 2016;5(3-4):218–31.
[10] Turner BN, Gold SA. A review of melt extrusion additive manufacturing processes: II. Materials, dimensional accuracy, and surface roughness. Rapid Prototyp J 2015.
[11] Kretzschmar N, Chekurov S, Salmi M, Tuomi J. Evaluating the readiness level of additively manufactured digital spare parts: an industrial perspective. Appl Sci 2018;8(10):1837.
[12] Chekurov S, Metsä-Kortelainen S, Salmi M, Roda I, Jussila A. The perceived value of additively manufactured digital spare parts in industry: an empirical investigation. Int J Prod Econ 2018;205:87–97.

[13] Akmal JS, Salmi M, Mäkitie A, Björkstrand R, Partanen J. Implementation of industrial additive manufacturing: intelligent implants and drug delivery systems. J Funct Biomater 2018;9(3):41.
[14] Tuomi J, Paloheimo K, Björkstrand R, Salmi M, Paloheimo M, Mäkitie AA. Medical applications of rapid prototyping-from applications to classification. Innovative Developments in Design and Manufacturing: Advanced Research in Virtual and Rapid Prototyping–Proceedings of VRAP, 4; 2009. p. 701–4.
[15] Mäkitie A, Paloheimo KS, Björkstrand R, Salmi M, Kontio R, Salo J, et al. Medical applications of rapid prototyping - three-dimensional bodies for planning and implementation of treatment and for tissue replacement. Duodecim 2010;126(2):143–51.
[16] Ramírez AS, D'Amato R, Haro FB, Marcos MI, Juanes JA. Novel technique based on fused filament fabrication (FFF) and robocasting to create composite medical parts. J Med Syst 2019;43(5):120.
[17] Giberti H, Strano M, Annoni M. An innovative machine for Fused Deposition Modeling of metals and advanced ceramics. MATEC Web of Conferences, EDP Sciences, 43; 2016. p. 03003.
[18] Thompson Y, Gonzalez-Gutierrez J, Kukla C, Felfer P. Fused filament fabrication, debinding and sintering as a low cost additive manufacturing method of 316L stainless steel. Addit Manuf 2019;30:100861.
[19] Ait-Mansour I, Kretzschmar N, Chekurov S, Salmi M, Rech J. Design-dependent shrinkage compensation modeling and mechanical property targeting of metal FFF. Prog Addit Manuf 2020;5(1):51–7.
[20] Singh P, Balla VK, Tofangchi A, Atre SV, Kate KH. Printability studies of Ti-6Al-4 V by metal fused filament fabrication (MF3). Int J Refract Hard Met 2020:105249.
[21] Agarwala MK, van Weeren R, Bandyopadhyay A, Whalen PJ, Safari A, et al. Fused deposition of ceramics and metals: an overview. 1996 International Solid Freeform Fabrication Symposium 1996.
[22] Agarwala MK, van Weeren R, Bandyopadhyay A, Safari A, Danforth SC, et al. Filament feed materials for fused deposition processing of ceramics and metals. 1996 International Solid Freeform Fabrication Symposium 1996.
[23] Guan X, Xu X, Kuniyoshi R, Zhou H, Zhu Y. Electromagnetic and mechanical properties of carbonyl iron powders-PLA composites fabricated by fused deposition modeling. Mater Res Express 2018;5(11):115303.
[24] Kukla C, Gonzalez-Gutierrez J, Burkhardt C, Weber O, Holzer C. The production of magnets by FFF-fused filament fabrication. In: Proceedings of the Euro PM2017 Congress & Exhibition; 2017.
[25] Vaezi M, Chianrabutra S, Mellor B, Yang S. Multiple material additive manufacturing–part 1: a review. Virtual Phys Prototyp 2013;8(1):19–50.
[26] Bandyopadhyay A, Heer B. Additive manufacturing of multi-material structures. Mater Sci Eng R Rep 2018;129:1–16.
[27] Kestilä A, Nordling K, Miikkulainen V, Kaipio M, Tikka T, Salmi M, et al. Towards space-grade 3D-printed, ALD-coated small satellite propulsion components for fluidics. Addit Manuf 2018;22:31–7.
[28] Sahasrabudhe H, Harrison R, Carpenter C, Bandyopadhyay A. Stainless steel to titanium bimetallic structure using LENS™. Addit Manuf 2015;5:1–8.
[29] Onuike B, Heer B, Bandyopadhyay A. Additive manufacturing of Inconel 718—copper alloy bimetallic structure using laser engineered net shaping (LENS™). Addit Manuf 2018;21:133–40.
[30] Heer B, Bandyopadhyay A. Compositionally graded magnetic-nonmagnetic bimetallic structure using laser engineered net shaping. Mater Lett 2018;216:16–9.
[31] Hofmann DC, Kolodziejska J, Roberts S, Otis R, Dillon RP, Suh J, et al. Compositionally graded metals: a new frontier of additive manufacturing. J Mater Res 2014;29(17):1899–910.
[32] Shishkovsky I, Missemer F, Smurov I. Direct metal deposition of functional graded structures in Ti-Al system. Phys Procedia 2012;39:382–91.
[33] Hofmann DC, Roberts S, Otis R, Kolodziejska J, Dillon RP, Suh J, et al. Developing gradient metal alloys through radial deposition additive manufacturing. Sci Rep 2014;4:5357.
[34] Tibbits S. 4D printing: multi-material shape change. Archit Des 2014;84(1):116–21.
[35] https://shop.thevirtualfoundry.com/collections/metal-filaments/products.
[36] Ruismäki R, Dańczak A, Klemettinen L, Taskinen P, Lindberg D, Jokilaakso A. Integrated battery scrap recycling and Nickel slag cleaning with methane reduction. Minerals (Basel) 2020;10(5):435.
[37] Mousapour M, Azadbeh M, Danninger H. Effect of compacting pressure on shape retention during supersolidus liquid phase sintering of Cu base alloys. Powder Metall 2017;60(5):393–403.
[38] Ghasemi S, Azadbeh M, Mousapour M, Mohammadzadeh A, Danninger H, Salimi N. The role of pore evolution during supersolidus liquid phase sintering of prealloyed brass powder. Powder Metall 2020;63(3):187–96.